The Lowest-frequency Fast Radio Bursts: Sardinia Radio Telescope Detection of the Periodic FRB 180916 at 328 MHz

M. Pilia[1], M. Burgay[1], A. Possenti[1,2], A. Ridolfi[1,3], V. Gajjar[4], A. Corongiu[1], D. Perrodin[1], G. Bernardi[5,6,7], G. Naldi[5], G. Pupillo[5], F. Ambrosino[8,9], G. Bianchi[5], A. Burtovoi[10,11], P. Casella[12], C. Casentini[8,13], M. Cecconi[14], C. Ferrigno[15], M. Fiori[16], K. C. Gendreau[17], A. Ghedina[14], G. Naletto[11,16], L. Nicastro[18], P. Ochner[11,16], E. Palazzi[18], F. Panessa[8], A. Papitto[12], C. Pittori[12,19], N. Rea[20,21], G. A. Rodriguez Castillo[12], V. Savchenko[15], G. Setti[5,22], M. Tavani[8,23], A. Trois[1], M. Trudu[1,2], M. Turatto[11], A. Ursi[8], F. Verrecchia[12,19], and L. Zampieri[11]

[1] INAF—Osservatorio Astronomico di Cagliari—via della Scienza 5—I-09047 Selargius, Italy; maura.pilia@inaf.it
[2] Università di Cagliari—Dipartimento di Fisica—S.P. Monserrato-Sestu Km 0,700-I-09042 Monserrato, Italy
[3] Max Planck Institute für Radioastronomie, Auf dem Hügel 69, D-53121 Bonn, Germany
[4] Department of Astronomy, University of California Berkeley, Berkeley CA 94720, USA
[5] INAF-Istituto di Radio Astronomia, via Gobetti 101, I-40129 Bologna, Italy
[6] Department of Physics and Electronics, Rhodes University, P.O. Box 94, Grahamstown, 6140, South Africa
[7] South African Radio Astronomy Observatory, Black River Park, 2 Fir Street, Observatory, Cape Town, 7925, South Africa
[8] INAF/IAPS, via del Fosso del Cavaliere 100, I-00133 Roma (RM), Italy
[9] Sapienza Università di Roma, Piazzale Aldo Moro 5, I-00185 Roma (RM), Italy
[10] Centre of Studies and Activities for Space (CISAS) "G. Colombo," University of Padova, Via Venezia 15, I-35131 Padova, Italy
[11] INAF—Osservatorio Astronomico di Padova—Vicolo dell'Osservatorio 5-I-35122 Padova, Italy
[12] INAF/OAR, via Frascati 33, I-00078 Monte Porzio Catone (RM), Italy
[13] INFN Sezione di Roma 2, via della Ricerca Scientifica 1, I-00133 Roma (RM), Italy
[14] Fundación Galileo Galilei—INAF—Rambla J.A.Fernández P. 7, E-38712, S.C.Tenerife, Spain
[15] ISDC, Department of Astronomy, University of Geneva, Chemin d'Écogia, 16 CH-1290 Versoix, Switzerland
[16] Department of Physics and Astronomy, University of Padova, Via F. Marzolo 8, I-35131, Padova, Italy
[17] Astrophysics Science Division, NASA Goddard Space Flight Center, Greenbelt, MD 20771, USA
[18] INAFOsservatorio di Astrofisica e Scienza dello Spazio di Bologna, Via Piero Gobetti 93/3, I-40129 Bologna, Italy
[19] SSDC/ASI, via del Politecnico snc, I-00133 Roma (RM), Italy
[20] Institute of Space Sciences (ICE, CSIC), Campus UAB, Carrer de Can Magrans s/n, E-08193, Barcelona, Spain
[21] Institut d'Estudis Espacials de Catalunya (IEEC), Carrer Gran Capità 2–4, E-08034 Barcelona, Spain
[22] Dipartimento di Fisica e Astronomia, Universitá di Bologna, Via Gobetti 93/2, I-40129 Bologna, Italy
[23] Università degli Studi di Roma "Tor Vergata," via della Ricerca Scientifica 1, I-00133 Roma (RM), Italy

Abstract

We report on the lowest-frequency detection to date of three bursts from the fast radio burst FRB 180916.J0158+65, observed at 328 MHz with the Sardinia Radio Telescope (SRT). The SRT observed the periodic repeater FRB 180916.J0158+65 for five days from 2020 February 20 to 24 during a time interval of active radio bursting, and detected the three bursts during the first hour of observations; no more bursts were detected during the remaining $\sim$30 hr. Simultaneous SRT observations at 1548 MHz did not detect any bursts. Burst fluences are in the range 37 to 13 Jy ms. No relevant scattering is observed for these bursts. We also present the results of the multi-wavelength campaign we performed on FRB 180916.J0158+65, during the five days of the active window. Simultaneously with the SRT observations, others with different time spans were performed with the Northern Cross at 408 MHz, with XMM-Newton, NICER, INTEGRAL, AGILE, and with the TNG and two optical telescopes in Asiago, which are equipped with fast photometers. XMM-Newton obtained data simultaneously with the three bursts detected by the SRT, and determined a luminosity upper limit in the 0.3–10 keV energy range of $\sim$$10^{45}$ erg s^{-1} for the burst emission. AGILE obtained data simultaneously with the first burst and determined a fluence upper limit in the MeV range for millisecond timescales of 10^{-8} erg cm^{-2}. Our results show that absorption from the circumburst medium does not significantly affect the emission from FRB 180916.J0158+65, thus limiting the possible presence of a superluminous supernova around the source, and indicate that a cutoff for the bursting mechanism, if present, must be at lower frequencies. Our multi-wavelength campaign sensitively constrains the broadband emission from FRB 180916.J0158+65, and provides the best limits so far for the electromagnetic response to the radio bursting of this remarkable source of fast radio bursts.

Unified Astronomy Thesaurus concepts: Radio transient sources (2008)

1. Introduction

Fast radio bursts (FRBs) are fast, millisecond-duration, extremely bright ($\sim$Jy) bursts that have so far only been observed at radio wavelengths. Their extragalactic nature has been confirmed by the first repeating FRB (RFRB), FRB 121102, located at a redshift of $z = 0.193$ (Spitler et al. 2014, 2016; Chatterjee et al. 2017; Marcote et al. 2017; Tendulkar et al. 2017). However, in the last year, observations

performed in the frequency band between 400 and 800 MHz by the Canadian Hydrogen Intensity Mapping Experiment (CHIME; CHIME/FRB Collaboration et al. 2018), led to a significant growth in the known population of "repeaters" (alternative name for RFRBs) (CHIME/FRB Collaboration et al. 2019a, 2019d; Fonseca et al. 2020).

Among the 20 RFRB sources published to date, FRB 180916.J0158+65 (hereafter FRB 180916; CHIME/FRB

Collaboration et al. 2019d) was discovered by CHIME through the detection of 10 bursts, with a flux density ranging from ∼0.4 to ∼4 Jy. A subsequent targeted VLBI campaign, favored due to the active nature of the source and its low extragalactic dispersion measure of DM ∼ 349 pc cm^{-3}, led to the identification of the host galaxy at a redshift $z = 0.0337$ (Marcote et al. 2020). The localization of FRB 180916, the second ever for an RFRB, immediately showed a dichotomy with the case of FRB 121102: indeed, the former was found in a star-forming region within a nearby massive spiral galaxy, at odds with the latter, which is hosted in a dwarf galaxy (Chatterjee et al. 2017; Marcote et al. 2017). The subsequent continuous monitoring of FRB 180916 by CHIME led to the first identification of a periodicity in the active phases of an RFRB (CHIME/FRB Collaboration et al. 2020, hereafter CF20) (now possibly also followed by the detection of a periodicity from the original repeater; Rajwade et al. 2020b). In particular, FRB 180916 displays a periodicity of 16.3 days in its phases of activity, with an active window phase concentrated within ±2.6 days around the midpoint of the window. Although it is still rather uncertain, the radio burst rate during the active window in the CHIME frequency band is ∼1.0 ± 0.5 hr^{-1}. The reported periodicity seems far too long to be ascribed to a neutron star's (NS) rotational frequency, unless FRB progenitors are older, ultra-long-period magnetars (Beniamini et al. 2020). This triggered a wealth of alternative hypotheses, such as orbital effects (Ioka & Zhang 2020; Lyutikov et al. 2020) or various kinds of precessional effects (Gu et al. 2020; Levin et al. 2020; Yang & Zou 2020; Zanazzi & Lai 2020), including the precession of a jet produced by intermediate black hole accretion (Katz 2020), or other secular semi-periodic cyclic phenomena, e.g., the source traveling across an asteroid belt (Dai & Zhong 2020). Most of these models revisited concepts developed for the modeling of the original RFRB (for a review see Platts et al. 2019), tuned to a ∼16 day periodicity.

From an observational point of view, the availability of predictable "windows for radio observations," in combination with the rare proximity of the source, makes FRB 180916 the best target for additional studies in the radio band, as well as for multi-wavelength follow-ups. We have exploited one of these windows (that centered on 2020 February 21) in order to search, with the Sardinia Radio Telescope (SRT; Bolli et al. 2015; Prandoni et al. 2017), for the signature of bursts at frequencies below 400 MHz, where no FRB nor RFRB has so far been detected (Houben et al. 2019; Rajwade et al. 2020a). In parallel, we set up observations at higher radio frequencies, as well as in the optical, X-ray, and γ-ray bands.

In Section 2 we describe the multi-wavelength campaign while in Section 3 we present the results, focused on the detection of three bursts at 328 MHz with the SRT, and on the upper limits (ULs) from the simultaneous observations at other wavelengths; in Section 4 we discuss the properties of the bursts and some implications resulting from this initial campaign.

2. Observations

We carried out a multi-wavelength campaign to look at FRB 180916 during its active cycle starting on 2020 February 19, centered on 2020 February 21 at 16:12 UT, and ending on 2020 February 24. The campaign was set up in order to maximize the overlap of the simultaneous observations between the radio
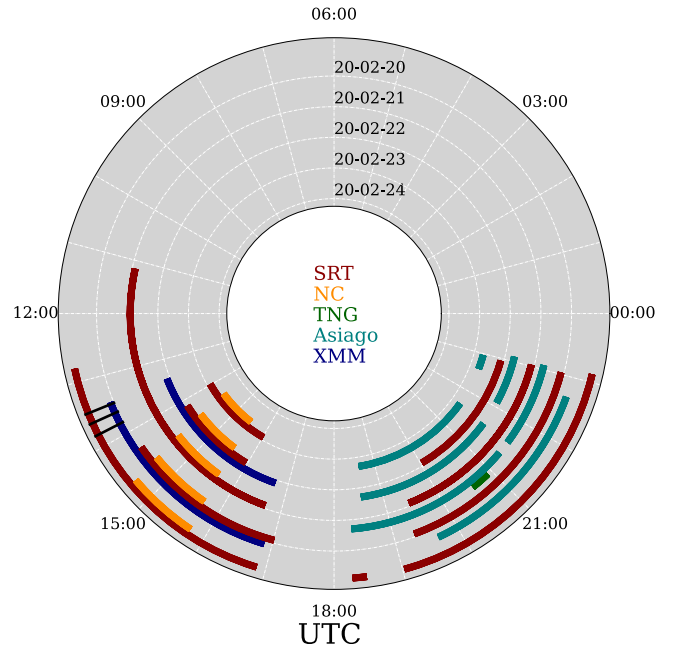

Figure 1. Observational multi-wavelength campaign around the SRT observations (red). Concentric circles represent different days. NICER, INTEGRAL, and AGILE were active during most of the SRT observing windows, except during epochs of visibility limitations (see the text for details). The three black radial segments between UTC 13:00 and 14:00 represent the three bursts.

observatories and the multi-wavelength instruments. Details of the observational campaign can be found in Figure 1.

2.1. Radio Observations

2.1.1. The SRT

The 64 m SRT observed FRB 180916 for a total of 30 hr over a time span of five days. Observations were performed using the L/P dual-band coaxial receiver (Valente et al. 2010), with the two observing bands centered at 1548 MHz (L-band) and 328 MHz (P-band), respectively. Observations in the L-band were performed with the ATNF Digital Filterbank Mark III backend (DFB[24]), with a bandwidth of 500, 1 MHz wide channels and a sampling time $t_s = 125\ \mu$s. Observations in the P-band were performed in baseband mode using the ROACH1 backend (Bassa et al. 2016), which acquired data over a 64 MHz bandwidth.

The modified radiometer formula for pulsars (Lorimer & Kramer 2004) applied to the SRT observations at L- and P-bands results in a minimum detectable flux density of 600 mJy and 2.2 Jy for a 1 ms burst, in the two bands, respectively. For the P-band we consider a 6σ limit. Given the presence of radio-frequency interference (RFI) in the L band, the actual useful bandwidth was reduced to 350 MHz. Wide-band RFI, which in some cases saturated the backend, was also present; to take its effects into account, we set a threshold limit of 10σ for L-band searches. The telescope gain in the two bands was $G_L = 0.55$ K Jy^{-1} and $G_P = 0.52$ K Jy^{-1}, respectively. The system temperatures, accounting for the antenna temperature and the sky temperature, as extrapolated from 408 MHz all-sky map (Reich & Reich 1988), were 30 K and 60 K, respectively.

---

[24] www.jb.man.ac.uk/pulsar/observing/DFB.pdf

2.1.2. The Northern Cross Radio Telescope

Observations with the Northern Cross (NC) radio telescope were carried out for seven days starting on 2020 February 19 and ending on 2020 February 25, for a total observing time of about 7.5 hr (1.1 hr per day). The system used to observe FRBs with the NC is described in Locatelli et al. (2020) and will be briefly summarized here. Six cylinders of the north–south arm were used for our observations. Each cylinder is composed of four receivers. Signals from the 24 receivers were calibrated by observing Cas A in interferometric mode, and then combined together in a single digital beam that followed the source as it transited across the field of view (FoV). Beam-formed voltages were stored to disk with a 138.24 μs time resolution over a 16 MHz bandwidth centered at 408 MHz, with a 12.2 kHz frequency resolution. The increased frequency resolution, compared to the 781 kHz used in Locatelli et al. (2020), was achieved by Fourier transforming each frequency channel in a time window of 64 points and led to negligible intrachannel smearing.

2.2. X-Ray/Gamma-Ray Observations

2.2.1. XMM-Newton

We obtained two XMM-Newton observations allocated as Director Discretionary Time (OBs 0854590701 and 0854590801). The observations were performed on 2020 February 20 (from 13:27 to 16:52) and on 2020 February 22 (from 13:26 to 16:43). These on-source UT times refer to the EPIC-pn instrument, which observed the target in full frame and thin filter, with a time resolution of 73.37 ms. The on-source times for the other instruments (Metal Oxide Semi-conductor (MOS) cameras in full mode, thin filter; Reflection Grating Spectrometer (RGS) in default spectroscopy mode; Optical Monitor (OM) in fast mode, U filter) vary only slightly. Data reduction was carried out with the SAS Data Analysis software version 17.0.0.

2.2.2. NICER

NICER observed FRB 180916 with several short observations over six days, to cover the predicted activity period of the target, obtained as Director Discretionary Time. A total of more than 113 ks were collected on source, with a sub-μs time resolution in the 0.2–12 keV energy range.

2.2.3. Integral

INTEGRAL observed FRB 180916 via a target of opportunity in search for a possible steady or impulsive hard X-ray/soft γ-ray counterpart to its radio emission. The INTEGRAL observations were interrupted by two spacecraft perigee passages, and were carried out from 2020 February 20 14:53:58 to 2020 February 21 05:12 UT, from 2020 February 21 15:38 to 2020 February 23 20:42 UT, and from 2020 February 24 06:39 to 2020 February 24 17:20:31 UT, for a total on-source time of 261 ks (three days).

All INTEGRAL data were processed using the standard INTEGRAL Offline Scientific Analysis (OSA) software, version 11.0.

2.2.4. AGILE

AGILE observed FRB 180916 with two detectors: the γ-ray imaging detector (GRID), which is sensitive in the range 30 MeV–30 GeV with a 2.5 sr FoV, and the Mini-Calorimeter (MCAL), which is sensitive in the 0.4–100 MeV band with 4π non-imaging acceptance (Tavani et al. 2009; Tavani 2019). AGILE is currently operating in spinning mode, with the instrument axis rotating every $\sim$7 min around the satellite–Sun direction. For each satellite revolution, a large fraction of the sky ($\sim$40%–60%) is exposed, depending on the Earth occultation pattern and trigger disabling over the South Atlantic anomaly (SAA, about 10% of the 95 min orbit). Over timescales of hours, $\sim$80% of the entire sky can be exposed by the GRID γ-ray imager and by the MCAL.

2.3. Optical Observations

2.3.1. SiFAP2/TNG

FRB 180916 was observed in the optical band with SiFAP2 (Ghedina et al. 2018) at the INAF's 3.58 m Telescopio Nazionale Galileo (TNG). Based on Silicon Photo Multiplier technology, SiFAP2 is composed of two Multi Pixel Photon Counter (MPPC) sensors working in the optical band ranging from 320 to 900 nm (Meddi et al. 2012; Ambrosino et al. 2016, 2017). Each sensor has a time-tagging capability of 8 ns and can integrate the number of incoming photons in adjustable time windows ranging from 100 ms down to 1 ms. A commercial Global Positioning System unit provides the absolute time with an accuracy that is better than 60 μs (Papitto et al. 2019) on the UTC. At the TNG focal plane, the FoV of each sensor is about 7×7 arcsec^2, ensuring that the sources are completely collected even in bad seeing conditions ($\sim$3″). The two MPPC detectors acquired simultaneously the target (FRB 180916) and the nearby sky background located at an angular distance of 4′ away from the target itself. The SiFAP2 observing run was carried out from 2020 February 21 20:35:02 to 2020 February 21 20:54:31 UT, for a total exposure time of roughly 1.2 ks. The acquisition was stopped because of bad weather conditions, ensuring only a short window (less than 20 min) of simultaneous observation with Aqueye+ (see Section 2.3.2) and the SRT.

2.3.2. Aqueye+ and IFI+Iqueye at Asiago

FRB 180916 was also observed with Aqueye+, which is mounted at the Copernicus telescope, and IFI+Iqueye, which is mounted at the Galileo telescope in Asiago, Italy. Aqueye+ and Iqueye[25] are fast photon counters with a FoV of 6″–12″ and the capability of time tagging the detected photons with sub-ns accuracy (Barbieri et al. 2009; Naletto et al. 2009, 2013; Zampieri et al. 2015). Iqueye is fiber-fed through a dedicated instrument (Iqueye Fiber Interface; Zampieri et al. 2019). We also performed simultaneous observations of the field in the Sloan i-band with a conventional CCD camera mounted on the 67/92 Schmidt telescope. Several (unfiltered) acquisitions were performed with Aqueye+ and IFI+Iqueye between 2020 February 20 and 23 (see Figure 1), for a total on-source time of $\sim$11.5 hr for Aqueye+ and $\sim$13.5 hr for IFI+Iqueye. The sky background was simultaneously and continuously monitored with the on-sky detector of Aqueye+ (approximately 10′ away from the target and with a FoV comparable to that of the on-source detectors). The average count rate measured with the on-source detectors was 2900–4300 counts s^{-1} for Aqueye+ and 1800–3200 counts s^{-1} for IFI+Iqueye. The data reduction

---

[25] https://web.oapd.inaf.it/zampieri/aqueye-iqueye/

Table 1
Properties of the Three Radio Bursts from FRB 180916 Detected by the SRT

Time (UT)	Time (MJD)	Width (ms)	S/N (⋯)	Peak flux (Jy)	Fluence (Jy ms)	DM (pc cm^{-3})
13:28:25.983(8)	58899.56141184	13(4)	31.7	2.8(9)	37(16)	349.8(1)
13:37:39.437(7)	58899.56781756	9(4)	13.6	1.5(7)	13(8)	349.4(1)
13:48:53.20(1)	58899.57561573	14(4)	16.0	1.4(4)	19(8)	350.1(1)

Note. Burst arrival times are barycentric at infinite frequency, i.e., after correcting for the DM delay at 328 MHz. All bursts were detected on 2020 February 20.

was performed with dedicated software. The whole acquisition and reduction chain ensures an absolute accuracy of ∼0.5 ns relative to UTC (Naletto et al. 2009).

3. Data Analysis and Results

3.1. Radio

3.1.1. SRT

L-band data were recorded at 2 bits per sample by the DFB as psrfits (Hotan et al. 2004) files; these were later converted to 8 bit filterbank files using SIGPROC[26] (Lorimer 2011). *P*-band data were acquired as dada baseband files and subsequently converted to 8 bit filterbank format using digifil (van Straten & Bailes 2011). The 64 MHz bandwidth was divided into 256, 250 Hz wide channels and the resulting 4 μs time resolution was then averaged down to 128 μs; the data were coherently dedispersed at the nominal DM = 348.82 pc cm^{-3} (CF20). The *P*-band channelized filterbank files were processed through the Python-based pipeline SPANDAK,[27] which is similar to that used in Gajjar et al. (2018). Data were first processed through rfifind from the PRESTO package[28] for high-level RFI purging. The pipeline uses Heimdall (Barsdell et al. 2012) as the main kernel to quickly search across a DM range from 300 to 400 pc cm^{-3}. Since Heimdall is unaware of the fact that the data are coherently dedispersed at the nominal DM of the source, we used a threshold of 0.01% for the maximum sensitivity loss for each given DM, so that the DM step would be 0.03 pc cm^{-3}, corresponding to a maximum DM smearing of 0.5 ms across the observing band. For the same reason, we used the option -no_scrunching to avoid time rebinning at the FRB's DM. The dedispersed time-series were searched for pulses using a matched-filtering technique with a maximum window size of 32.8 ms. Each candidate found by Heimdall was scrutinized against all other candidates for each given observation to validate and identify only the genuine ones. The pipeline produced around 7000 candidates at different DMs. All candidates with DM between 340 and 360 pc cm^{-3} were visually inspected; we identified three clear bursts from the observations at 328 MHz on 2020 February 20, which will be discussed below. As a cross-check, we also analyzed the *P*-band data using PRESTO over 121 DM values covering the range 345.82–351.82 pc cm^{-3}. A slightly different approach was used for RFI excision, where only the frequency channels affected by strong RFI were removed through the -ignorechan option of the PRESTO's pre-psubband routine. The option -noclip was also used during dedispersion to avoid strong bursts being flagged as RFI. The python code single_pulse_search.py was

used with a signal-to-noise ratio (S/N) threshold of 6, a maximum width of 38.4 ms, and the option -b to avoid checking for bad blocks (potentially saving strong pulses from being discarded). The only good single pulses found were the same three as detected by the SPANDAK pipeline. The remaining candidates were all monochromatic bursts of RFI.

L-band observations were analyzed using the same pipeline as the *P*-band observations and, given the large amount of RFI, using the single pulse search from PRESTO on a small DM range around the nominal value. In particular, the data were first cleaned from RFI using rfifind, then dedispersed with prepsubband using 12 DM values from 346.32 to 351.82. The resulting time series were analyzed with single_pulse_search.py using an S/N threshold of 10 and a maximum width of 37.5 ms. All of the resulting candidates were visually inspected and recognized as RFI.

In summary, the SRT detected three radio bursts from FRB 180916 in the *P*-band on 2020 February 20. It is interesting to note that this is the first firm detection of an FRB below 400 MHz. Detection of nine bursts at 111 MHz has been reported by Fedorova & Rodin (2019). However, the observational setup of their system (a coarse frequency resolution of 78 kHz over a tiny observing bandwidth of 2.5 MHz, and a sampling time not faster than 12.5 ms) required the use of a template-matching approach in order to see the bursts. Although the authors do their best to support the validity of this methodology, its use is very limited so far in the context of FRB searches, and the statistics of the false-positive is not completely assessed. Moreover, the claimed detection is very hard to reconcile with the stringent limits imposed by all other non-detections at similar frequencies, derived using well consolidated procedures (Coenen et al. 2014; Karastergiou et al. 2015; Tingay et al. 2015; Sokolowski et al. 2018; Chawla et al. 2020). Properties of these bursts are summarized in Table 1. No simultaneous bursts (taking into account the DM delay between the two bands) were detected blindly in the *L*-band data, down to a limiting sensitivity of $600 \times (W \text{ ms}^{-1})^{-0.5}$ mJy, where W is the pulse width in ms. By analyzing the relevant data segments, the limit can be moved down to $360 \times (W \text{ ms}^{-1})^{-0.5}$ mJy, with a 6σ threshold.

3.1.2. DM Optimization and Burst Structures

FRBs are known to show complex burst structures with multiple burst components. Many of the RFRBs and non-RFRBs have been shown to exhibit a drifting emission pattern where emission gradually moves from higher to lower frequencies across the leading component to consecutive trailing components. Gajjar et al. (2018) showed that these burst structures can superimpose for different trial DMs, which could lead to incorrect DM estimations. As shown in Figure 2, all of our detected bursts show a single component. However, it is possible that our observations were not sensitive enough to
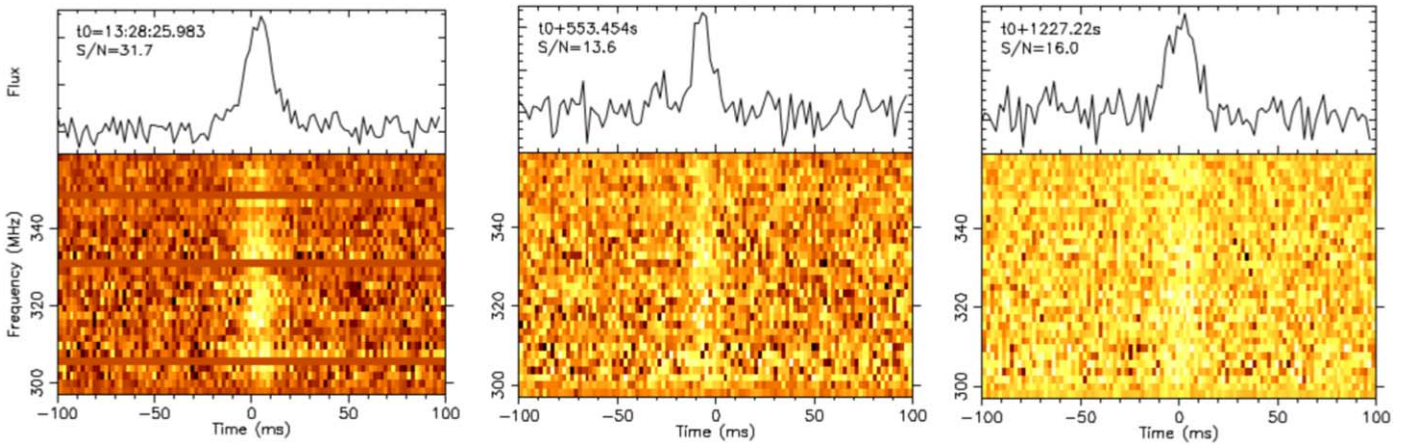

Figure 2. Profiles of the three bursts observed by the SRT. The upper panels represent the pulse profile in arbitrary flux units; the lower panels show the dynamic spectra of the bursts, here scrunched into 32 frequency channels. Horizontal blank lines represent channels zapped due to RFI.

resolve these underlying structures. One of the ways to reveal such structures is to estimate "structure-maximizing DM"—DM where all sub-burst structures spanning different frequencies arrive at the same time. This structure-maximizing DM can then be compared with the S/N-maximizing DM (DM where the S/N of integrated burst profile peaks). If there are underlying structures, they are likely to superimpose to give higher S/N-maximizing DM compared to the structure-maximizing DM (see Figure 1 in Gajjar et al. 2018).

Two different techniques have been proposed to estimate the structure-maximizing DM. CHIME/FRB Collaboration et al. (2019c) suggested a coherent summation of Fourier transformed spectra taken across channels for the burst, while Gajjar et al. (2018) suggested maximizing the forward time-derivative of the burst profile. For weaker burst pulses, Hessels et al. (2019) suggested a second-order forward derivative, while Josephy et al. (2019) suggested a fourth-order forward derivative. Here, we carried out a comparison between S/N-maximizing DMs and structure-maximizing DMs across a range of trial DMs for our brightest detected burst (i.e., burst-1). To estimate the structure-maximizing DM, we found that the second-order derivative was able to provide a single prominent peak. Figure 3 shows the comparison of S/N-maximizing DMs with structure-maximizing DMs for burst-1. We did not find any significant difference between these two DMs within the measurement uncertainties. Thus, we confirm the absence of any underlying sub-burst structure for our detected bursts. This could also be due to our limited observing bandwidth. For example, burst number 2 (from day 181019) from FRB 180916 appears to show two components where the frequency span of each sub-burst structure is around 100 MHz CHIME/FRB Collaboration et al. (2019a), which is larger than the bandwidth of our observations.

3.1.3. Northern Cross

Single-beam, channelized observations were analyzed following a pipeline similar to the SRT case and based on the `Heimdall` code. Observations, which were not simultaneous with the SRT detected bursts, achieved a 3 $(W\,ms^{-1})^{-0.5}$ Jy 6σ rms sensitivity at 408 MHz. No burst was detected in the 7.5 hr of the campaign.
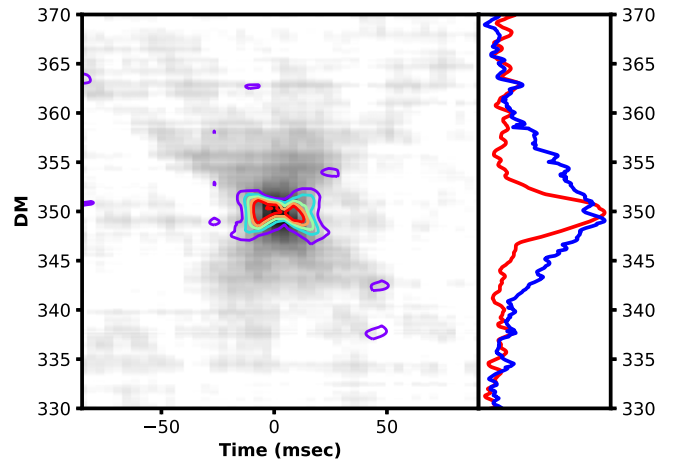

Figure 3. Comparison of S/N-maximizing DMs with the structure-maximizing DMs for burst-1 detected across 300–360 MHz at the SRT. The left panel shows the S/N in the gray-scale intensities as a function of DM vs. time in the background. The standard "butterfly" pattern is clearly visible with a peak in the middle. The overlaid contours (with levels at 0.35, 0.5, 0.6, 0.7, and 0.8 times the peak) are from the structure-maximizing parameter intensities. The right panel shows the normalized average intensities from a −20 to +20 ms region around the peak; blue and red lines represent S/N and structure parameter as a function of DM, respectively. The original data, with a temporal resolution of 244 μs and a spectral resolution of 7.8 khz, were first averaged to obtain temporal and spectral resolution of 4 ms and 1 MHz, respectively. We also used a uniform 2D filter of size 0.1 pc cm^{-3} × 11 ms to smooth the intensities. A Gaussian function was fitted for both average intensities in the right-hand panel. We found an S/N-maximizing DM of 350.1(0.3) pc cm^{-3} and a structure-maximizing DM of 349.8(0.1) pc cm^{-3}. Here, uncertainties were obtained from standard deviations of DM and S/N intensities from the off-pulse and after propagating them during Gaussian fitting.

3.2. X-Ray and Gamma-Ray Observations

XMM-Newton: we focused on the data obtained by the EPIC-pn, since it had the largest effective area among the available instruments, and offered the best time resolution (73.3 ms compared to 2.7 s for the EPIC-MOS cameras). We only considered the first hour of the first observations, during which the SRT detected the three bursts reported here; it was the only time in which the observations were not affected by a high flaring particle background. We extracted good events, singles and doubles (`PATTERN` ⩽ 4) with an energy range between 0.3 and 10 keV. We extracted a region of 25″ around

Table 2
Average AGILE/MCAL Fluence ULs in erg cm^{-2}

sub-ms	1 ms	16 ms	64 ms	256 ms	1024 ms	8192 ms
1.13×10^{-8}	1.29×10^{-8}	3.72×10^{-8}	4.97×10^{-8}	7.95×10^{-8}	1.59×10^{-7}	4.49×10^{-7}

the position of FRB 180916, while different background regions were extracted on source-free parts of the same CCD, and then back-scaled to the dimension of the on-source extraction. At the position of the source, we counted 30.0 ± 5.5 photons in 3.2 ks, which is compatible with the average of 31.8 ± 0.9 background photons. The corresponding UL on the background-subtracted average count rate, evaluated for a 3σ confidence level, is $5.8 \times 10^{-3}\,\mathrm{s}^{-1}$ (see Gehrels 1986). We assumed a spectral model typical of magnetar steady emission (see, e.g., Rea et al. 2008), composed of a blackbody (with $kT = 0.5$ keV) and a power-law component (with $\Gamma = 3$), and an absorption column of 4.3×10^{21} cm^{-1} evaluated from the Galactic H I Column Density maps in the source direction with the Heasoft NH tool. Under these assumptions, we estimated an upper limit on the unabsorbed *persistent* flux of $6 \times 10^{-14}\,\mathrm{erg\,cm}^{-2}\,\mathrm{s}^{-1}$ (0.3–10 keV). At a luminosity distance of 149 Mpc, this corresponds to $\sim 1.5 \times 10^{41}\,\mathrm{erg\,s}^{-1}$.

A search for any impulsive or nearly impulsive excess at or close to the times of the three bursts yielded no significant detection. The closest in time X-ray photon from the source position lagged the third observed radio burst by ~ 8 s. We evaluated ULs of $90.3\,\mathrm{s}^{-1}$ and $6.6\,\mathrm{s}^{-1}$ on the count rate in each of the 73 ms bins coincident with radio detections, and within an interval of 1 s, respectively. Assuming a spectrum typical of soft gamma repeater (SGR) bursts (see, e.g., Israel et al. 2008), composed of two blackbody components with temperatures $kT_1 = 3$ and $kT_2 = 7$ keV, and the absorption column reported above, we derived an upper limit on the unabsorbed *burst-like* (0.3–10 keV) flux of $2.2 \times 10^{-9}\,\mathrm{erg\,cm}^{-2}\,\mathrm{s}^{-1}$ and of $1.6 \times 10^{-10}\,\mathrm{erg\,cm}^{-2}\,\mathrm{s}^{-1}$ for the first and second radio detections. These correspond to luminosity limits to the X-ray counterparts of the two bursts of $\sim 5.5 \times 10^{45}\,\mathrm{erg\,s}^{-1}$ and $\sim 4 \times 10^{44}\,\mathrm{erg\,s}^{-1}$.

We note that by loosening the filtering criteria, namely including the lowest energies, a cluster of photons is detected at a position that is marginally consistent with the target, at UT time 2020 February 20 13:31:56 (barycentered to the solar system using DE-405 ephemerides), which would correspond to either a few minutes before the first SRT burst, or a few minutes after the second SRT burst. However, careful inspection of the data reveals that the detected photons form a clear track on the detector. We conclude that they are caused by the interaction of an energetic particle with the detector.

NICER: NICER was not pointing at the target at the times SRT detected the three bursts reported here, because of viewing limitations. A search for impulsive events yielded no significant detection through the whole data set. Further deeper searches are ongoing and the results will be presented in future publications.

INTEGRAL: all three radio bursts reported in this paper occurred between ~ 1 and ~ 1.5 hr before the start of the INTEGRAL pointing observation, and no deep ULs could be obtained close to the time of the discovered events. Using INTEGRAL all-sky detectors, we derive a 3σ UL on a 75–2000 keV fluence of any burst shorter than 1 s (50 ms) of $1.8 \times 10^{-7}\,\mathrm{erg\,cm}^{-2}$ ($4 \times 10^{-8}\,\mathrm{erg\,cm}^{-2}$) anywhere within

± 300 s from the radio bursts. In addition, we searched for any short magnetar-like bursts in the entire INTEGRAL/ISGRI observation, and did not detect any, setting a 3σ UL on 28–80 keV fluence in 1 s at the level of $2.3 \times 10^{-8}\,\mathrm{erg\,cm}^{-2}$, and on fluence in less than 100 ms at the level of $6.1 \times 10^{-9}\,\mathrm{erg\,cm}^{-2}$.

Integrating over the entire INTEGRAL exposure time, we do not detect any steady emitting source at the position of FRB 180916. We derive a 3σ UL on the average flux of $3.1 \times 10^{-11}\,\mathrm{erg\,cm}^{-2}\,\mathrm{s}^{-1}$ in the 28–80 keV energy range (with IBIS/ISGRI), and $2.3 \times 10^{-11}\,\mathrm{erg\,cm}^{-2}\,\mathrm{s}^{-1}$ in the 3–10 keV range (with JEM-X).

AGILE: the AGILE/MCAL on-board data acquisition is based on a trigger logic acting on different energy ranges and timescales (ranging from $\sim 300\,\mu$s to ~ 8 s). A detailed discussion on MCAL triggering and UL capabilities in the context of FRB studies is reported in Casentini et al. (2020) and Ursi et al. (2019).

We searched for MCAL triggered events at or near the radio bursts. Our search was within ± 100 s from the arrival times of Table 1. MCAL collected useful data only for burst-1. For the other two events, the AGILE satellite was in the SAA region, and no MCAL data could be obtained. No significant event was detected in temporal coincidence with burst-1. The MeV fluence UL obtained for a millisecond timescale trigger is $F'_{\mathrm{MeV,UL}} = 10^{-8}\,\mathrm{erg\,cm}^{-2}$. Table 2 shows the MCAL fluence ULs at different trigger timescales. The value at 1 s corresponds to an isotropic MeV luminosity of $L_{\mathrm{MeV,UL}} = 3.4 \times 10^{46}\,\mathrm{erg\,s}^{-1}$.

The analysis of γ-ray GRID data is based on the standard AGILE-GRID multi-source likelihood analysis (Bulgarelli et al. 2012), which takes into account nearby known γ-ray sources and the diffuse Galactic emission at the FRB 180916 location ($l = 129.7$, $b = 3.7$). For this campaign, we obtained γ-ray flux ULs for different integrations: (1) a 100 s integration centered at the burst time of event-1; (2) a 5 day integration covering a complete activity cycle of FRB 180916 (2020 February 19–24); (3) a 30 day interval that also included the previous cycle (2020 February 4–8) during which AGILE was observing simultaneously with Swift (Tavani et al. 2020b). The corresponding UL values are: $F_{\gamma,\mathrm{UL}} = 2.7 \times 10^{-7}\,\mathrm{erg\,cm}^{-2}\,\mathrm{s}^{-1}$ for the 100 s integration above 50 MeV; $F_{\gamma,\mathrm{UL}} = 1.4 \times 10^{-10}\,\mathrm{erg\,cm}^{-2}\,\mathrm{s}^{-1}$ for the 5 day integration above 100 MeV, and $F_{\gamma,\mathrm{UL}} = 2.7 \times 10^{-11}\,\mathrm{erg\,cm}^{-2}\,\mathrm{s}^{-1}$ for the 30 day integration above 100 MeV. The last value corresponds to an isotropic long-term averaged γ-ray luminosity $L_{\gamma,\mathrm{ave,UL}} \sim 7.2 \times 10^{43}\,\mathrm{erg\,s}^{-1}$.

3.3. Optical

The optical telescopes did not observe simultaneously with the detected radio bursts, which happened during the daytime.

SiFAP2: to derive an upper limit for the other slots of observation in this campaign, we considered the ratio between the count rate observed from the source position and from the sky background. This smoothed out the effect of quickly varying atmospheric conditions that characterized the sky during the observations. We did not detect any impulsive signal above a sensitivity threshold of 38.6 counts per 1 ms long bin

(3σ confidence level after taking into account for the number of trials). This corresponds to a magnitude of $V \sim 15.3\text{--}15.5$.

Aqueye+ and IFI+Iqueye: we performed a systematic search for any significant increase in the count rate on 1 ms binned light curves of the optical observations (not background subtracted). We did not detect any simultaneous on-source radio–optical burst. Considering the average rate and the number of trials, the limiting sensitivity for the detection of a 1 ms pulse at the $\sim 3\sigma$ confidence level in an observation of 1 hr duration is 19–23 counts/bin for Aqueye+ and 15–20 counts/bin for Iqueye, corresponding to an instantaneous (1 ms) magnitude $V = 13.4\text{--}13.7$ (fluence 0.012–0.016 Jy ms) for Aqueye+ a $V = 11.7\text{--}12$ (fluence 0.060–0.079 Jy ms) for Iqueye.

Standard data reduction was applied to the simultaneous Schmidt images. No event was detected in any of the images down to a limiting magnitude $i = 20$ (fluence 7.9 Jy ms for a 5 min exposure).

4. Discussion

4.1. Temporal Distribution of the Bursts

The SRT observed for a total of 30.3 hr. The three bursts were observed within a 20 min interval at phase ~ 0.43 of the active period, which peaks at phase 0.5. No other bursts were detected at P-band during the remainder of the campaign and no bursts at all were detected throughout the whole campaign at L-band. Given our nominal sensitivity, we expect that we would have been able to detect at least three of the four bursts detected by Effelsberg at L-band in Marcote et al. (2020).

Assuming a Poissonian distribution of the events in the ± 2.6 days of activity of the source, and with the hypothesis that our sensitivity did not change during the time span of the observations, except for a little variation of the RFI environment, we calculated the probability that our detections all occurred during the first hour of observations. If we assume the rate of ~ 1 burst hr^{-1} from CF20, we obtain a probability $P(3) = 4 \times 10^{-10}$ that the SRT should observe only three bursts during the full time span of its observations, and obviously the probability is even lower for the three bursts to all occur within a 20 min interval. While it is true that no fluence completeness distribution can be derived for the SRT at the moment, and that the two instruments have different sensitivity limits, the aforementioned probabilities seem to discard a uniform distribution of bursts at 328 MHz along the ~ 5.2 day window; they favor a clustering of the bursting activity of FRB 180916, as also hinted at by CHIME observations. Zanazzi & Lai (2020) propose that this clustering is expected in the framework of their precessing magnetar model. This is because the viewing angle of an observer constantly changes phase with respect to the NS's inclination angle due to precession, and the intensity of the bursts changes accordingly.

4.1.1. Scattering

We investigated the possible presence of a scattering tail in the observed profiles by comparing them to simulated scattered ones. The code we used to generate the simulated profiles was designed for radio pulsar profile investigations, and requires, as a reference, an observed profile at a frequency that is high enough to be unaffected by this phenomenon. In this case, given the lack of such a reference profile, we assumed that the
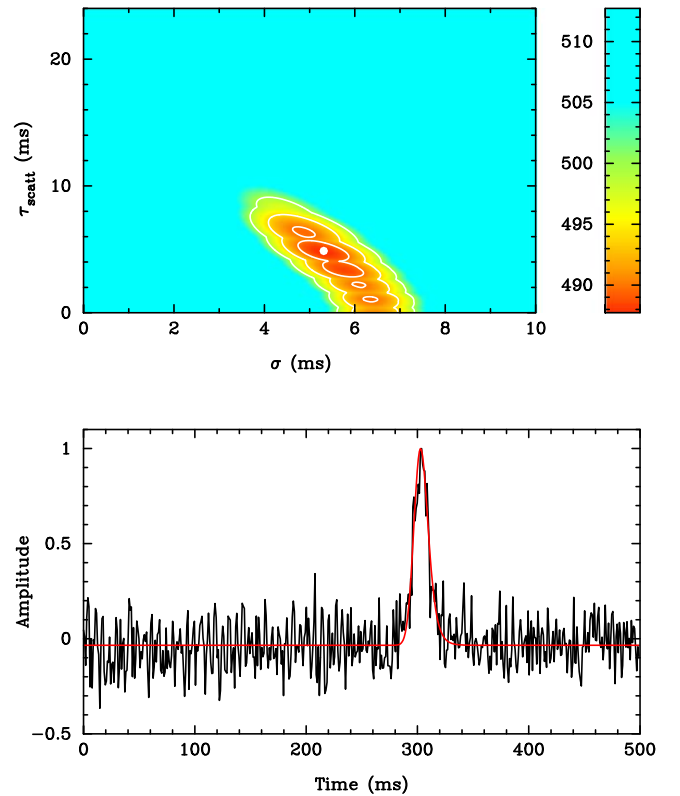

Figure 4. Upper panel: left: $\sigma_G - \tau_S$ χ^2 color map for burst-1; the white dot indicates the $\sigma_G - \tau_S$ couple of values for which χ^2 is minimum; the white lines trace the contour levels at 1, 2, and 3σ, moving away from the white dot. Right: reference color scale for the χ^2 color map. Lower panel: burst-1 profile resolved in 512 time bins along the displayed 0.5 s of data. The red superposed line is the simulated scattered profile that results from the couple of values $\sigma_G - \tau_S$ for which the χ^2 is minimum. Both profiles have been normalized to have zero average and peak amplitude 1.

unscattered profile is well approximated by a Gaussian curve. We then exploited the 2D $\sigma_G - \tau_S$ space, where σ_G is the unknown width of the unscattered Gaussian, and τ_S is the scattering time at our observing frequencies. We compared the simulated profile corresponding to each couple $\sigma_G - \tau_S$ to the observed one, and assigned a χ^2 value to each of them:

$$\chi^2(\sigma_G, \tau_S, \phi_0) = \int_0^1 [S(\sigma_G, \tau_S, \phi - \phi_0) - P(\phi)]^2 d\phi \quad (1)$$

where $S(\sigma_G, \tau_S, \phi)$ is the simulated profile, $P(\phi)$ is the observed one, and ϕ_0 is the phase shift between the two profiles for which $\chi^2(\sigma_G, \tau_S, \phi_0)$ is minimum. The upper panel of Figure 4 displays the resulting χ^2 map for burst-1 along with the 1, 2, and 3σ contour levels. The lower panel shows the observed profile resolved in 512 bins along the displayed 0.5 s of data with, superimposed, the simulated scattered profile that results from the couple of values $\sigma_G - \tau_S$ for which the χ^2 is minimum. The resulting χ^2 maps for each of the three bursts indicate that the 2σ ULs for τ_S at 328 MHz are 9.5 ms, 10.2 ms and 10.8 ms for burst-1, -2, and -3, respectively.

Once rescaled to the reference frequency of 1 GHz, they imply $\tau_S \leqslant 0.1$ ms, under the hypothesis $\tau_S \propto \nu^{-4}$ (where ν is the radio frequency). This result fits in nicely with the DM$-\tau_S$ correlation reported by CHIME/FRB Collaboration et al. (2019b), in their Figure 2.

7

It is worth noting that inspection of the $\sigma_G - \tau_S$ χ^2 maps shows that the three SRT bursts are also compatible with being immune to (or having a very low level of) scattering, which means that detection at frequencies that are even lower than the SRT P-band might be possible. For instance, a value of $\tau_S \sim$ 1 ms at 328 MHz would translate to modest scattering delays ($\sim$10–20 ms) at frequencies around 150–190 MHz, which are typical of the LOFAR high band (Stappers et al. 2011; van Haarlem et al. 2013). On the other hand, for τ_S values approaching the ULs reported above, the burst energy would be diluted over 0.8–1.0 s, easily causing the non-detection of similar bursts with LOFAR (Houben et al. 2019). Therefore, additional future observations of the periodic FRB 180916 at P-band (where the feasibility is now warranted) are needed to collect events that are bright enough to finally constrain the value of τ_S. This is particularly crucial for assessing the role played in FRB science—at least for nearby sources—by future low-frequency telescopes, such as SKA-LOW, which will be operating in the 50–350 MHz band.

4.2. Spectral Properties of the Radio Bursts

Several explanations were proposed to explain the lack of detection of FRBs or RFRBs at low frequencies. Ravi & Loeb (2019) suggested that free–free absorption by electrons in the intervening medium or, alternatively, induced Compton scattering can be responsible for the non-detections below 400 MHz (Chawla et al. 2017; Sokolowski et al. 2018; Rajwade et al. 2020a). Rajwade et al. (2020a), in particular, showed that induced Compton scattering alone cannot account for the lack of detections in their 332 MHz FRB survey. They suggest that free–free absorption should play a more prominent role, most likely happening in post-shock regions of super-luminal supernovae where the electron densities can reach $n_e \sim 10^5$ cm^3 (Margalit & Metzger 2018). Sokolowski et al. (2018) reached similar conclusions, although without discriminating between physical absorption models. The FRB 180916 case is a peculiar example of the opposite scenario, where the three bursts are seen at 328 MHz but are undetected at 1.4 GHz, revealing the absence of a spectral turnover.

Barring any specific modeling, the detection of three bursts at 328 MHz confirms that (R)FRB environments can be optically thin to this emission and that a cutoff for the bursting mechanism, if present, must be at even lower frequencies. Although FRBs have not yet shown simultaneous emission over a wide radio-frequency band, simultaneous radio observations in two widely separate bands—as shown here—can be extremely valuable for constraining the instantaneous apparent spectral properties of the bursts. In fact, it is worth noting that the observed spectrum of FRBs is likely significantly affected by the effects of the medium the signal went across (see, e.g., Cordes et al. 2017; Cordes & Chatterjee 2019) and hence might not map the intrinsic spectral properties of the source.

Our single-frequency detection does not allow us to place constraints on any specific physical mechanisms, but our detection threshold is comparable to that of Rajwade et al. (2020b), indicating that the environment of a superluminal supernova (SN) seems unlikely for this source—even though it is located in a star-forming region (Marcote et al. 2020). The absence of a bright SN is consistent with the fact that Marcote et al. do not find accompanying persistent emission to FRB

180916 down to a limiting sensitivity that is 400 times lower than the detected emission of FRB 121102. In particular, the non-detection at L-band allows us to set a UL on the burst spectral index[29] $\alpha \sim 1$ for the brightest burst, assuming the nominal L-band sensitivity. A modulation due to plasma lenses (Cordes et al. 2017) remains an open possibility, although the lack of simultaneous detection at 1.4 GHz makes it not obvious; a future, dedicated analysis will be required.

4.3. Burst Energetics

The total (assumed isotropic) energy $E_{r,\,i}$ emitted in the observed radio band during a radio burst can be approximated as

$$E_{r,i} \simeq 2.7 \times 10^{37} \, S_{\nu,\text{Jy}} \, \delta t \, \Delta \nu \, d_{150M}^2 \text{ erg,} \qquad (2)$$

where S_ν is the measured FRB peak flux density in Jy, δt is the duration of the burst in ms, $\Delta\nu$ is the bandwidth in GHz, and $d_{150M} = d/150$ Mpc, with d the source distance from Earth. For burst-1 from the SRT, $S_\nu = 2.8$ Jy, $\delta t = 13$ ms, and $\Delta\nu = 0.064$ GHz, resulting in $E_{r,i} \simeq 6.3 \times 10^{37}$ erg.

Where does this energy output come from? The plethora of proposed theoretical models about the emission mechanism(s)—and hence the energetics—of RFRBs mainly rely on the observed properties of the original source, FRB 121102. In particular, most hypotheses invoke a relatively young magnetar spinning at a millisecond period, whose radio bursting activity might be powered by its high magnetic field and resulting from either internal processes or triggered by the interaction with an extreme magneto-ionic environment (see, e.g., Beloborodov 2017; Margalit & Metzger 2018).

As reported in Section 1, similar considerations could be applied to the case of FRB 180916, once suitably adjusted to explain its periodicity. However, there are also significant differences between the properties of the two RFRBs (e.g., the nature of the host galaxy; Chatterjee et al. 2017; Marcote et al. 2017; Tendulkar et al. 2017; Marcote et al. 2020; the rotation measure; Gajjar et al. 2018; Michilli et al. 2018, CF20), which may lead us to explore other possibilities, such as the idea (see, e.g., Cordes & Wasserman 2016) of a predominant role of the spin-down power of an NS in shaping the energetics of FRB 180916. In fact, emission from pulsar giant pulses (considered as a manifestation of the conversion of rotational energy into coherent bright radio emission), as observed for instance from the Crab pulsar (see, e.g., Hankins & Eilek 2007; Mickaliger et al. 2012), was proposed by some authors (Lyutikov et al. 2016) as a favored emission mechanism for the FRB, as compared to a magnetic-powered scenario, on the basis of both the energetics and other properties of the pulsar giant pulses (i.e., polarization, spectra) that are reminiscent of what is seen in FRBs.

The energy of burst-1 is several orders of magnitude above the typical energy of the Crab's giant pulses (see, e.g., Hankins et al. 2003; Mickaliger et al. 2012). However, it was noted (Cordes & Wasserman 2016) that millisecond-duration emission can be the result of the coherent addition of nanosecond-shot emission, similarly to the strongest examples observed in the Crab pulsar, in which unresolved 0.4 ns bursts of $S_{\text{peak}} \sim 2$ MJy have been detected (Hankins & Eilek 2007). Cordes & Wasserman (2016) suggested that a much longer monitoring

---

[29] We use the convention $F_\nu \propto \nu^{-\alpha}$, where F_ν is the flux density at the frequency ν.

of the Crab pulsar with respect to that available so far could show the occurrence of ultra-giant pulses with energetics comparable to those of FRBs. In addition, much brighter pulses could be released by an NS that is younger and more energetic than the Crab.

This hypothesis would in turn call for the FRB 180916's source to be enshrouded in a SN remnant. Piro (2016) studied this case and noted that the reverse shock, produced by the SN ejecta when they encounter the interstellar medium, generates free electrons that can disperse and absorb the radio signal. Hence, emission down to ~300 MHz can escape from free–free absorption only when the intervening matter is diluted enough, i.e., at least 300–500 yr after the SN explosion, depending on the density of the medium and, mostly, on the mass of the ejecta. Following this model (Figure 5 of Piro 2016), and assuming the usually invoked formulae relating P and $\dot{P}$ to the age and the surface magnetic field of an NS (see, e.g., Lorimer & Kramer 2004), the energy released by burst-1 could originate from the spin-down power of an NS of age larger than about 300 yr, spin period of a few ms, and surface magnetic field $B \leqslant 10^{11}$ G. This picture could be validated by the observation of a progressively decreasing dispersion measure associated with the pulses over the next few years.

Very recent developments in the field are showing that a border land may be connecting the two aforementioned energy sources for the RFRBs, which might also be simultaneously at work. In 2020 March, Esposito et al. (2020) observed the just discovered (Enoto et al. 2020), and possibly also the youngest (Champion et al. 2020), Galactic magnetar, Swift-J1818.0–1607. Seven days after the occurrence of an X-ray burst, which is usually interpreted as a magnetic-powered event, an observation with the SRT showed that the radio emission from Swift-J1818.0–1607 (in turn discovered shortly after the X-ray burst; Karuppusamy et al. 2020), was at that time predominantly occurring in the form of strong and sporadic radio pulses. In 2020 April, the already known Galactic magnetar SGR J1935+2154 was observed by Swift (Palmer 2020), soon followed by many X-ray instruments, to produce a forest of X-ray bursts. Four days later, Scholz & CHIME/FRB Collaboration (2020) reported a single millisecond-duration radio burst observed by CHIME and coming from the same source with an estimated fluence of ~kJy ms; it was also independently detected by STARE2 (Bochenek et al. 2020) at L-band, with an estimated fluence >1.5 MJy ms. Despite extensive radio follow-ups, at the date of writing, only one other burst has been reported since then: it was observed by FAST six days after the original X-ray event, with an estimated fluence of 60 mJy ms at L-band (Zhang et al. 2020a). While these radio bursts, from an energetics point of view, are all still not bright enough to match the more energetic FRBs, this is the closest we have come so far to directly associating a class of known sources (magnetars and pulsars), as well as of emission properties (X-ray bursts and very strong radio pulses), to a phenomenology resembling that of RFRBs.

4.4. The Multi-wavelength Campaign and Constraints to Models

Figure 5 shows a summary of the millisecond-fluence ULs obtained using the instruments involved in our campaign. XMM-Newton and AGILE were active at the time of the detected bursts and therefore their ULs, together with the SRT's L-band, constitute a punctual limit on the high-energy
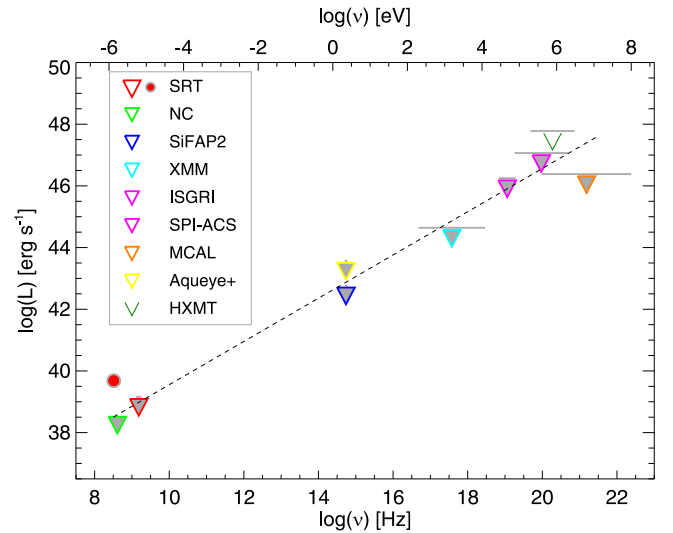

Figure 5. Burst luminosity vs. frequency diagram throughout the electromagnetic spectrum for the observations performed during our multiwavelength campaign. The red dot represents the SRT burst-1 detection; the remaining gray-filled triangles represent ULs obtained on the millisecond-fluence by the instruments involved in our campaign that can have sensitivity in the millisecond range. SRT L-band observation, XMM-Newton, and AGILE-MCAL were simultaneous with the detection of burst-1, while the other gray-filled triangles represent the sensitivity limits probed by the instruments that did not have simultaneous observations with the SRT bursts. SRT L-band data and the NC data refer to a 13 ms burst and the ULs are calculated at the 6σ level, as is standard for the radio band, as opposed to the 3σ ULs indicated for the multi-wavelength counterparts. INTEGRAL SPI-ACS data refer to a 50 ms limit, as specified in the text (Section 3.2). The dark green, unfilled triangle represents the corresponding UL reached by HXMT using archival data (Guidorzi et al. 2020). The black dashed line with slope 0.70 is not a fit and is only intended as a guide for the eye.

emission from the SRT bursts. The ULs displayed for the NC and the optical telescopes are, on the other hand, an estimate of the sensitivity reached by our survey. For comparison, we show the Hard X-ray Modulation Telescope (HXMT) UL that was recently published in Guidorzi et al. (2020).

Simultaneous X-ray observations with XMM-Newton in the X-ray range led to upper limits on the persistent and burst luminosities, of ~10^{41} and ~10^{45} erg s^{-1}, respectively (under the assumptions for the spectral shapes reported in Section 3.2). In the case of an isolated young pulsar scenario, this persistent limit is not constraining, given that the typical X-ray luminosities of a young rotational powered pulsar or a magnetar are $<10^{38}$ erg s^{-1}. As for the bursting luminosity, we can compare the ULs related to the available XMM, INTEGRAL, and AGILE data (see below) to check the level at which ultra-energetic events can be constrained.

X-ray and hard X-ray observations with INTEGRAL (not simultaneous with the SRT radio bursts) on 0.1–1 s timescales provide ULs to the fluence in the range $(0.6 - 2) \times 10^{-8}$ erg cm^{-2} s^{-1}, and therefore an UL on the total energy in the range $(1-4) \times 10^{46}$ erg.

As for AGILE, we focus on burst-1, which has the largest radio fluence among those detected by the SRT. AGILE/MCAL provides an interesting UL in the MeV range simultaneously with this radio detection. The value of F' translates into a UL for the isotropically radiated energy into the MeV range, $E_{\mathrm{MeV,UL}} = 4\pi F' d_{150M}^2 \simeq (2.2 \times 10^{46}\,\mathrm{erg})\,d_{150M}^2$. This value of $E_{\mathrm{MeV,UL}}$ should be compared with the energy emitted in the

radio band, $E_{r,i} \simeq 6.3 \times 10^{37}$ erg. Therefore, our UL on the energy emitted in the MeV range on millisecond timescales is less than $\sim 5 \times 10^8$ times the energy emitted at 328 MHz for this radio burst.

It is interesting to compare the various high-energy ULs reported above with the energy emitted by SGR 1806–20 (e.g., Turolla et al. 2015) during its giant outburst in 2004, which lasted about 200 ms (Hurley et al. 2005; Palmer et al. 2005), while burst-1 lasted ~ 20 ms. In that case, an isotropic energy $E_{MeV} \sim (2 \times 10^{46}$ erg) was emitted in the MeV range. We can thus exclude, as a counterpart to burst-1 in X-rays, a giant burst that is at least twice as bright as SGR 1806–20. INTEGRAL, AGILE, Konus-Wind, and HXMT (Mereghetti et al. 2020; Ridnaia et al. 2020; Tavani et al. 2020a; Zhang et al. 2020b) most recently detected the hard X-ray counterpart to the radio burst from SGR J1935+2154 observed by CHIME and STARE2. The preliminary estimated fluence of the high-energy burst, compared to the radio one, indicates that current telescope sensitivities might still be too high to detect high-energy emission even from relatively close FRBs such as FRB 180916.

During the reviewing stages of this manuscript, the results of a multi-wavelength campaign involving the Chandra X-ray telescope observing FRB 180916 simultaneously with CHIME were reported by Scholz et al. (2020). Their conclusions agree with our findings.

5. Summary

Our multi-wavelength observations of FRB 180916 provide a wealth of valuable information on this puzzling source. The SRT detection of three strong radio bursts at 328 MHz represents the first firm detection of any FRB type at such low frequencies. It also shows that no significant scattering is affecting the emission at these frequencies. On one hand, this confirms that the scattering time and DM seem to correlate (CHIME/FRB Collaboration et al. 2019a; Cordes & Chatterjee 2019); on the other hand, this leaves open a detection of (at least relatively nearby) FRBs at even lower frequencies with instruments such as LOFAR and SKA-LOW. The lack of a simultaneous detection at 1.5 GHz is also relevant: it confirms the narrowband emission typically seen from RFRBs, indicating either a relatively steep spectrum of the intrinsic radio emission or a strong effect of the intervening medium.
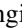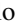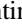
The source is capable of emitting $\sim 10^{38}$ erg within a few tens of milliseconds at 328 MHz, which is an energy many orders of magnitude larger than the giant pulses from Crab-like pulsars. In addition, the upper limits resulting from our simultaneous observation in the keV–MeV range for the first radio burst detected by the SRT are still compatible with high-energy activity that is similar to the 2004 giant outburst of SGR 1806–20. Additional upper limits obtained from our non-simultaneous observations in the optical, X-ray, hard X-ray, and γ-ray energy ranges constrain the emission of the FRB 180916 source to be less than 10^6–10^8 times the Eddington luminosity for a one solar-mass compact object.

The periodicity of the bursting activity of FRB 180916 represents an unprecedented observational opportunity to characterize its properties. Given the erratic behavior—from optical to high-energy frequencies—that is expected in the various proposed models, long-term radio monitoring at low and intermediate frequencies, as well as deep observations with the best available instruments across the electromagnetic spectrum, might finally allow us to determine the nature of the source and strongly constrain the mechanism of burst production.

ORCID iDs

M. Pilia ● https://orcid.org/0000-0001-7397-8091
M. Burgay ● https://orcid.org/0000-0002-8265-4344
A. Possenti ● https://orcid.org/0000-0001-5902-3731
A. Ridolfi ● https://orcid.org/0000-0001-6762-2638
V. Gajjar ● https://orcid.org/0000-0002-8604-106X
A. Corongiu ● https://orcid.org/0000-0002-5924-3141
D. Perrodin ● https://orcid.org/0000-0002-1806-2483
G. Bernardi ● https://orcid.org/0000-0002-0916-7443
G. Naldi ● https://orcid.org/0000-0003-1807-6188
G. Pupillo ● https://orcid.org/0000-0003-2172-1336
F. Ambrosino ● https://orcid.org/0000-0001-7915-996X
A. Burtovoi ● https://orcid.org/0000-0002-8734-808X
P. Casella ● https://orcid.org/0000-0002-0752-3301
C. Casentini ● https://orcid.org/0000-0001-8100-0579
C. Ferrigno ● https://orcid.org/0000-0003-1429-1059
M. Fiori ● https://orcid.org/0000-0002-7352-6818

A. Ghedina ⬤ https://orcid.org/0000-0003-4702-5152
G. Naletto ⬤ https://orcid.org/0000-0003-2007-3138
L. Nicastro ⬤ https://orcid.org/0000-0001-8534-6788
P. Ochner ⬤ https://orcid.org/0000-0001-5578-8614
E. Palazzi ⬤ https://orcid.org/0000-0002-8691-7666
F. Panessa ⬤ https://orcid.org/0000-0003-0543-3617
A. Papitto ⬤ https://orcid.org/0000-0001-6289-7413
C. Pittori ⬤ https://orcid.org/0000-0001-6661-9779
N. Rea ⬤ https://orcid.org/0000-0003-2177-6388
G. A. Rodriguez Castillo ⬤ https://orcid.org/0000-0003-3952-7291
V. Savchenko ⬤ https://orcid.org/0000-0001-6353-0808
M. Tavani ⬤ https://orcid.org/0000-0003-2893-1459
A. Trois ⬤ https://orcid.org/0000-0002-3180-6002
M. Trudu ⬤ https://orcid.org/0000-0002-1530-0474
M. Turatto ⬤ https://orcid.org/0000-0002-9719-3157
A. Ursi ⬤ https://orcid.org/0000-0002-7253-9721
F. Verrecchia ⬤ https://orcid.org/0000-0003-3455-5082
L. Zampieri ⬤ https://orcid.org/0000-0002-6516-1329

References

Ambrosino, F., Cretaro, P., Meddi, F., et al. 2016, JAI, 5, 1650005
Ambrosino, F., Papitto, A., Stella, L., et al. 2017, NatAs, 1, 854
Barbieri, C., Naletto, G., Occhipinti, T., et al. 2009, JMOp, 56, 261
Barsdell, B. R., Bailes, M., Barnes, D. G., & Fluke, C. J. 2012, MNRAS, 422, 379
Bassa, C. G., Janssen, G. H., Karuppusamy, R., et al. 2016, MNRAS, 456, 2196
Beloborodov, A. M. 2017, ApJL, 843, L26
Beniamini, P., Wadiasingh, Z., & Metzger, B. D. 2020, arXiv:2003.12509
Bochenek, C., Kulkarni, S., Ravi, V., et al. 2020, ATel, 13684, 1
Bolli, P., Orlati, A., Stringhetti, L., et al. 2015, JAI, 4, 1550008
Bulgarelli, A., Chen, A. W., Tavani, M., et al. 2012, A&A, 540, A79
Casentini, C., Verrecchia, F., Tavani, M., et al. 2020, ApJL, 890, L32
Champion, D., Desvignes, G., Jankowski, F., et al. 2020, ATel, 13559, 1
Chatterjee, S., Law, C. J., Wharton, R. S., et al. 2017, Natur, 541, 58
Chawla, P., Andersen, B. C., Bhardwaj, M., et al. 2020, ApJL, 896, L41
Chawla, P., Kaspi, V. M., Josephy, A., et al. 2017, ApJ, 844, 140
CHIME/FRB Collaboration, Amiri, M., Andersen, B. C., et al. 2020, arXiv:2001.10275
CHIME/FRB Collaboration, Amiri, M., Bandura, K., et al. 2018, ApJ, 863, 48
CHIME/FRB Collaboration, Amiri, M., Bandura, K., et al. 2019a, Natur, 566, 235
CHIME/FRB Collaboration, Amiri, M., Bandura, K., et al. 2019b, Natur, 566, 230
CHIME/FRB Collaboration, Andersen, B. C., Bandura, K., et al. 2019c, ApJL, 885, L24
CHIME/FRB Collaboration, Andersen, B. C., et al. 2019d, arXiv:1908.03507
Coenen, T., van Leeuwen, J., Hessels, J. W. T., et al. 2014, A&A, 570, A60
Cordes, J. M., & Chatterjee, S. 2019, ARA&A, 57, 417
Cordes, J. M., & Wasserman, I. 2016, MNRAS, 457, 232
Cordes, J. M., Wasserman, I., Hessels, J. W. T., et al. 2017, ApJ, 842, 35
Dai, Z. G., & Zhong, S. Q. 2020, ApJL, 895, L1
Enoto, T., Sakamoto, T., Younes, G., et al. 2020, ATel, 13551, 1
Esposito, P., Rea, N., Borghese, A., et al. 2020, ApJL, in press (arXiv:2004.04083)
Fedorova, V. A., & Rodin, A. E. 2019, ARep, 63, 877
Fonseca, E., Andersen, B. C., Bhardwaj, M., et al. 2020, ApJL, 891, L6
Gajjar, V., Siemion, A. P. V., Price, D. C., et al. 2018, ApJ, 863, 2
Gehrels, N. 1986, ApJ, 303, 336
Ghedina, A., Leone, F., Ambrosino, F., et al. 2018, Proc. SPIE, 10702, 107025Q
Gu, W.-M., Yi, T., & Liu, T. 2020, arXiv:2002.10478
Guidorzi, C., Marongiu, M., Martone, R., et al. 2020, A&A, 637, A69

Hankins, T. H., & Eilek, J. A. 2007, ApJ, 670, 693
Hankins, T. H., Kern, J. S., Weatherall, J. C., & Eilek, J. A. 2003, Natur, 422, 141
Hessels, J. W. T., Spitler, L. G., Seymour, A. D., et al. 2019, ApJL, 876, L23
Hotan, A. W., van Straten, W., & Manchester, R. N. 2004, PASA, 21, 302
Houben, L. J. M., Spitler, L. G., ter Veen, S., et al. 2019, A&A, 623, A42
Hurley, K., Boggs, S. E., Smith, D. M., et al. 2005, Natur, 434, 1098
Ioka, K., & Zhang, B. 2020, arXiv:2002.08297
Israel, G. L., Romano, P., Mangano, V., et al. 2008, ApJ, 685, 1114
Josephy, A., Chawla, P., Fonseca, E., et al. 2019, ApJL, 882, L18
Karastergiou, A., Chennamangalam, J., Armour, W., et al. 2015, MNRAS, 452, 1254
Karuppusamy, R., Desvignes, G., Kramer, M., et al. 2020, ATel, 13553, 1
Katz, J. I. 2020, MNRAS, 494, L64
Levin, Y., Beloborodov, A. M., & Bransgrove, A. 2020, ApJL, 895, L30
Locatelli, N. T., Bernardi, G., Bianchi, G., et al. 2020, MNRAS, 494, 1229
Lorimer, D. R. 2011, SIGPROC: Pulsar Signal Processing Programs, Astrophysics Source Code Library, ascl:1107.016
Lorimer, D. R., & Kramer, M. 2004, Handbook of Pulsar Astronomy (Cambridge: Cambridge Univ. Press)
Lyutikov, M., Barkov, M., & Giannios, D. 2020, ApJL, 893, L39
Lyutikov, M., Burzawa, L., & Popov, S. B. 2016, MNRAS, 462, 941
Marcote, B., Nimmo, K., Hessels, J. W. T., et al. 2020, Natur, 577, 190
Marcote, B., Paragi, Z., Hessels, J. W. T., et al. 2017, ApJL, 834, L8
Margalit, B., & Metzger, B. D. 2018, ApJL, 868, L4
Meddi, F., Ambrosino, F., Nesci, R., et al. 2012, PASP, 124, 448
Mereghetti, S., Savchenko, V., Gotz, D., et al. 2020, GCN, 27668, 1
Michilli, D., Seymour, A., Hessels, J. W. T., et al. 2018, Natur, 553, 182
Mickaliger, M. B., McLaughlin, M. A., Lorimer, D. R., et al. 2012, ApJ, 760, 64
Naletto, G., Barbieri, C., Occhipinti, T., et al. 2009, A&A, 508, 531
Naletto, G., Barbieri, C., Verroi, E., et al. 2013, Proc. SPIE, 8875, 88750D
Palmer, D. M. 2020, ATel, 13675, 1
Palmer, D. M., Barthelmy, S., Gehrels, N., et al. 2005, Natur, 434, 1107
Papitto, A., Ambrosino, F., Stella, L., et al. 2019, ApJ, 882, 104
Piro, A. L. 2016, ApJL, 824, L32
Platts, E., Weltman, A., Walters, A., et al. 2019, PhR, 821, 1
Prandoni, I., Murgia, M., Tarchi, A., et al. 2017, A&A, 608, A40
Rajwade, K. M., Mickaliger, M. B., Stappers, B. W., et al. 2020a, MNRAS, 493, 4418
Rajwade, K. M., Mickaliger, M. B., Stappers, B. W., et al. 2020b, MNRAS, 495, 3551
Ravi, V., & Loeb, A. 2019, ApJ, 874, 72
Rea, N., Zane, S., Turolla, R., Lyutikov, M., & Götz, D. 2008, ApJ, 686, 1245
Reich, P., & Reich, W. 1988, A&AS, 74, 7
Ridnaia, A., Golenetskii, S., Aptekar, R., et al. 2020, ATel, 13688, 1
Scholz, P. & CHIME/FRB Collaboration 2020, ATel, 13681, 1
Scholz, P., Cook, A., Cruces, M., et al. 2020, arXiv:2004.06082
Sokolowski, M., Bhat, N. D. R., Macquart, J. P., et al. 2018, ApJL, 867, L12
Spitler, L. G., Cordes, J. M., Hessels, J. W. T., et al. 2014, ApJ, 790, 101
Spitler, L. G., Scholz, P., Hessels, J. W. T., et al. 2016, Natur, 531, 202
Stappers, B. W., Hessels, J. W. T., Alexov, A., et al. 2011, A&A, 530, A80
Tavani, M. 2019, RLSFN, 30, 1
Tavani, M., Barbiellini, G., Argan, A., et al. 2009, A&A, 502, 995
Tavani, M., Ursi, A., Verrecchia, F., et al. 2020a, ATel, 13686, 1
Tavani, M., Verrecchia, F., Casentini, C., et al. 2020b, ApJL, 893, L42
Tendulkar, S. P., Bassa, C. G., Cordes, J. M., et al. 2017, ApJL, 834, L7
Tingay, S. J., Trott, C. M., Wayth, R. B., et al. 2015, AJ, 150, 199
Turolla, R., Zane, S., & Watts, A. L. 2015, RPPh, 78, 116901
Ursi, A., Tavani, M., Verrecchia, F., et al. 2019, ApJ, 871, 27
Valente, G., Pisanu, T., Bolli, P., et al. 2010, Proc. SPIE, 7741, 774126
van Haarlem, M. P., Wise, M. W., Gunst, A. W., et al. 2013, A&A, 556, A2
van Straten, W., & Bailes, M. 2011, PASA, 28, 1
Yang, H., & Zou, Y.-C. 2020, ApJL, 893, L31
Zampieri, L., Naletto, G., Barbieri, C., et al. 2015, Proc. SPIE, 9504, 95040C
Zampieri, L., Naletto, G., Barbieri, C., et al. 2019, CoSka, 49, 85
Zanazzi, J. J., & Lai, D. 2020, ApJL, 892, L15
Zhang, C. F., Jiang, J. C., Men, Y. P., et al. 2020a, ATel, 13699, 1
Zhang, S. N., Tuo, Y. L., Xiong, S. L., et al. 2020b, ATel, 13687, 1